Nozue and Fukahata
Earth, Planets and Space (2025) 77:12
https://doi.org/10.1186/s40623-024-02115-3

Earth, Planets and Space

FULL PAPER

Open Access

Geodetic data inversion to estimate a strain-rate field by introducing sparse modeling

Yohei Nozue[1*] and Yukitoshi Fukahata[2]

Abstract

Many studies have estimated crustal deformation from observed geodetic data. So far, because most studies have applied a smoothness constraint, which includes the assumption of local uniformity of a strain-rate field, localized strain rates near fault zones have tended to be underestimated when we invert spatially sporadic GNSS data. To overcome this difficulty, we introduce sparse modeling into the estimation of a strain-rate field. Specifically, we impose a sparsity constraint as well as the smoothness constraint on strain rates as prior information, which are expressed by the L1-norm and the L2-norm of the second-order derivative of the velocity field, respectively. To investigate the validity and limitation of the proposed method, we conduct synthetic tests, in which we consider an anti-plane strain problem due to a steady slip on a buried strike-slip fault. As a result, we find: (1) regardless of the locking depth of the fault, the proposed method reproduces localized strain rates near the fault with almost equal or better accuracy than the L2 regularization method (i.e., only the smoothness constraint); (2) the advantage of the proposed method over the L2 regularization method is clearer when data coverage is worse (i.e., when fewer observation points are available); and (3) the proposed method can be applied when observation errors are small. Next, we apply the proposed method to the GNSS data across the Arima-Takatsuki fault zone, which is one of the most active strike-slip faults in Japan. As a result, the proposed method estimates about 1.0×10^{-8}/yr faster strain rates near the fault zone than the L2 regularization method, which corresponds to a 20–30% greater strain-rate concentration. The faster strain rates result in the estimation of a shallower locking depth: 11 km by the proposed method, compared to 17 km by the L2 regularization method. The former is closer to the depth of D90, 12–14 km, above which 90% of earthquakes occur.

Keywords GNSS, Strain-rate field, Sparse modeling, Elastic net, Sparsity and smoothness

*Correspondence:
Yohei Nozue
nozue.youhei.74w@st.kyoto-u.ac.jp
Full list of author information is available at the end of the article

Graphical Abstract

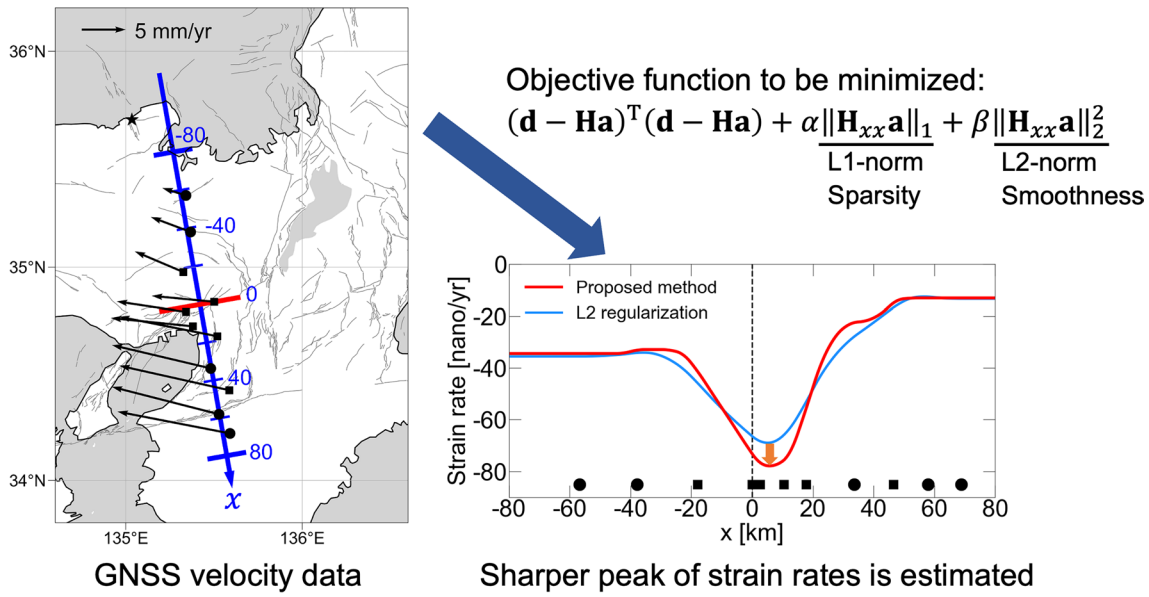

1 Introduction

Active seismicity and crustal deformation are observed in the Japanese Islands. Oceanic plates subduct beneath continental plates along the Japan Trench and Nankai Trough (Fig. 1), where large interplate earthquakes have occurred, such as the 2011 Tohoku-oki earthquake. The Japanese Islands also have many active faults, where large intraplate earthquakes have occurred, such as the 2024 Noto Peninsula earthquake (Okuwaki et al. 2024). Besides periodic deformations caused by stick-and-slip movements along plate boundaries, the Japanese Islands have been significantly deformed over a long period of time under the tectonics of E–W compression (e.g., Huzita 1980; Terakawa and Matsu'ura 2010).

Geodetic data provide fundamental information to better understand seismic activities and the development of geological structures. Since the 1990s, the Global Navigation Satellite System (GNSS) has enabled us to monitor crustal displacements. Today, more than 1300 observation stations, called the GNSS Earth Observation Network System (GEONET), operated by the Geospatial Information Authority of Japan (GSI) are installed all over Japan at intervals of about 20 km (Tsuji et al. 2017), and the displacement at each station for a certain time period can be obtained. Strain, which is the spatial derivative of displacement, more directly relates to seismic activities and the development of geological structures. Therefore, estimation of a strain-rate field from spatially sporadic geodetic data has been an important problem (Sagiya et al. 2000; Okazaki et al. 2021; Nishimura 2022).

Sagiya et al. (2000) estimated the strain-rate field of Japan from GNSS data using the method of Shen et al. (1996), which estimates a velocity field and a strain-rate field simultaneously by assuming a local uniformity of a strain-rate field; they found a strain-rate concentration zone named the Niigata-Kobe Tectonic zone (NKTZ) in central Japan (Fig. 1). Probably because the method of Shen et al. (1996) is easy to implement, it has been used by many studies (e.g., Meneses-Gutierrez and Sagiya 2016; Nishimura 2017; Fukahata et al. 2020) to estimate strain-rate fields. However, the method has some problems theoretically. It cannot objectively determine the parameter called the Distance Decaying Constant (DDC), which controls the range of uniformity of a strain-rate field, although its value significantly changes estimated strain-rate fields. It is also pointed out that the obtained strain-rate field does not coincide with the spatial derivative of the obtained velocity field (Okazaki et al. 2021).

Recently, using a basis function expansion under a framework of Bayesian inversion (Fukahata et al. 1996), Okazaki et al. (2021) estimated the strain-rate field of Japan from GNSS data for 4 years from 2006 to 2009. In Bayesian inversion, prior information as well as observed data is generally used. In Okazaki et al. (2021), the smoothness of the velocity field was used as prior information, which was expressed by the minimization of the

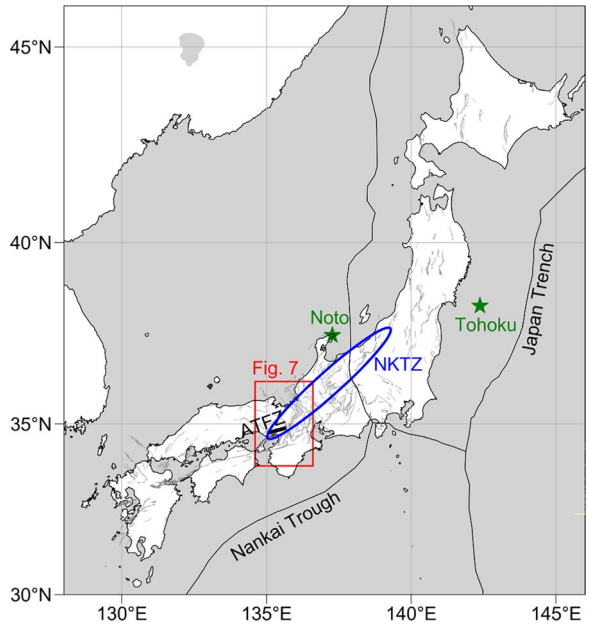

Fig. 1 Tectonic setting around the Japanese Islands. The thin black and gray lines represent the plate boundaries (Bird 2003) and active faults (The Geological Survey of Japan, National Institute of Advanced Industrial Science and Technology 2023), respectively. The bold black line and blue ellipse represent the locations of the Arima-Takatsuki fault zone (ATFZ) and the Niigata-Kobe Tectonic Zone (NKTZ), respectively. The region of Fig. 7 is shown by the red rectangle. The epicenters of the 2011 Tohoku-oki earthquake and the 2024 Noto Peninsula earthquake are also shown by green stars

L2-norm of the spatial derivative of a strain-rate field. The optimal weight between the prior information and observed data was objectively determined by Akaike's Bayesian Information Criterion (ABIC) (Akaike 1980). Using the same method, Fukahata et al. (2022) further estimated strain-rate fields for the periods of 1997–1999 and 2017–2020. The estimated strain-rate fields have higher resolution with reasonable uncertainty in comparison with previous studies including Sagiya et al. (2000). However, due to the smoothness constraint on a velocity field, we cannot exclude the possibility that the method using L2 regularization underestimates strain rates localized in narrow zones such as fault zones, even if we take the interval of basis functions to be sufficiently small.

On the other hand, localized strain rates along fault zones have been estimated by using a block-fault model (Matsu'ura et al. 1986). Nishimura et al. (2018) estimated deformation fields by dividing southwest Japan into 14 blocks based on GNSS data and the surface traces of active faults, in which it was assumed that surface deformation of each block is expressed as a sum of rigid block motions, uniform deformation, and interseismic elastic deformation due to locked faults on block boundaries. As a result, localized high slip rates were obtained along some active faults including the Arima-Takatsuki fault zone (ATFZ) (Fig. 1). However, there is arbitrariness in block division, which directly controls obtained results. In addition, because internal deformation in each block is mapped to block boundaries, the obtained deformation on block boundaries tends to be overestimated.

To overcome these difficulties, we introduce sparse modeling (compressed sensing) into geodetic data inversion to estimate a strain-rate field. Sparse modeling is a technique to effectively obtain characteristic amounts even from a small number of observed data. Tibshirani (1996) proposed a regression method called least absolute shrinkage and selection operator (LASSO), which is a basic type of sparse modeling shrinking many unknown model parameters to zero by imposing the minimization of the L1-norm of model parameters as a prior constraint. As addressed by Zou and Hastie (2005), however, LASSO has some limitations: for example, if there is a high correlation among some of variables to be estimated, LASSO tends to select only one variable among them and make the others zero. Zou and Hastie (2005) proposed a new method of sparse modeling called elastic net, which imposes the minimization of both the L1-norm and the L2-norm of model parameters as prior constraints, making a solution smoother than that of LASSO, while keeping sparsity.

Sparse modeling has been typically used in reproducing images from observed data. For example, Lustig et al. (2007) reproduced the distribution of brain blood vessels in high resolution from a smaller number of data by applying sparse modeling. Since active faults also distribute linearly like brain blood vessels, and the spatial density of GNSS stations is not enough to estimate a strain-rate field in high resolution, sparse modeling would be a powerful tool to estimate a strain-rate field from GNSS data. It should be noted that the interval of GNSS stations (about 20 km) is similar to the width of the strain concentration zones. In the field of geodetic data inversion, Evans and Meade (2012) imposed an L1-constraint in estimating the coseismic and afterslip distributions of the 2011 Tohoku-oki earthquake. Imposing both the L1- and L2-constraints on a slip distribution, Nakata et al. (2016) successfully reproduced an afterslip distribution with a sharp boundary by a synthetic test. Nakata et al. (2017) and Hori et al. (2018) further applied a similar model to observed GNSS data to estimate the slip distribution of a slow slip event. Yano and Kano (2022) applied an L1 trend filtering to GNSS time series in the Nankai subduction zone and detected new 12 slow slip event candidates.

In the following, we first formulate a geodetic data inversion to estimate a strain-rate field from GNSS data using sparse modeling, specifically an elastic net. For

simplicity, we consider the anti-plane strain problem. Next, based on numerical experiments, in which crustal deformation associated with steady slip on a buried strike-slip fault is modeled, we show the validity and limitation of the proposed method by comparing the results with those of the L2 regularization method. Finally, by applying the proposed method to observed GNSS data, we estimate a strain-rate profile across the Arima-Takatsuki fault zone, which is one of the most active strike-slip faults in Japan.

2 Method

2.1 Geometry of anti-plane strain problem

In the synthetic test (Sect. 3), we consider an anti-plane strain problem, for simplicity. The setting of the anti-plane strain problem is explained in this subsection. In the anti-plane strain problem, surface displacements are associated with a steady slip on a buried strike-slip fault whose length is infinite in the directions of the fault strike and the depth (Fig. 2). The y-axis is taken along the fault strike, and the x -axis is perpendicular to it. We consider surface displacements to the y-direction along the x-axis. As shown in Fig. 2, we assume the fault plane is locked from the surface to depth D and a steady slip occurs at a rate of s below this locking depth. The solution for the surface displacement in this setting is given by Savage and Burford (1970). In addition to this buried fault motion, we assume that the velocity profile has a uniform spatial gradient μ along the x-axis

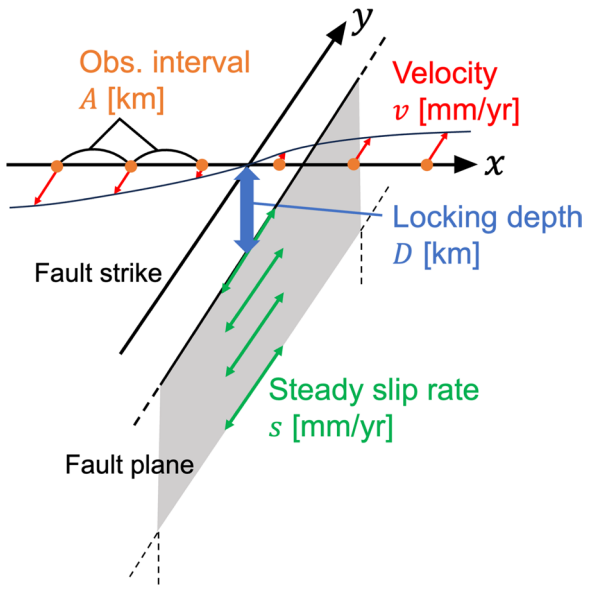

Fig. 2 Settings of an anti-plane strain problem. We consider a buried vertical strike-slip fault, whose length is infinite in the directions of the fault strike and depth. The fault slips at a constant rate s below the locking depth D. The y-axis is set along the fault strike, and the x-axis is perpendicular to it. We consider the surface velocity to the y direction along the x-axis, $v(x)$. A is the interval between observation points

considering factors such as plate subduction. Then, the true value of surface velocity $v(x)$ and shear strain rate $\dot{e}(x)$ are given as:

$$v(x) = \frac{s}{\pi}\tan^{-1}\left(\frac{x}{D}\right) + \mu x, \tag{1}$$

$$\dot{e}(x) = \frac{1}{2}\frac{\mathrm{d}v}{\mathrm{d}x} = \frac{sD}{2\pi}\frac{1}{x^2 + D^2} + \frac{\mu}{2}. \tag{2}$$

We place N observation points on the x-axis with an approximately constant interval $A(= 160/N)$ (Fig. 2). Let $\mathbf{x} = (x_1, \ldots, x_N)^{\mathrm{T}}$ be a vector containing the coordinates of observation points. The velocity data at these points are expressed as:

$$\mathbf{d} = (v_1, \ldots, v_N)^{\mathrm{T}} = \frac{s}{\pi}\tan^{-1}\left(\frac{\mathbf{x}}{D}\right) + \mu\mathbf{x} + \varepsilon, \tag{3}$$

where we assume ε follows a Gaussian noise with mean 0 and variance $\sigma^2\mathbf{I}$.

2.2 Estimation of a strain-rate field with L2 regularization

First, we explain a method to estimate a strain-rate field based on the basis function expansion with ABIC, in which only an L2 regularization is imposed as a prior constraint (Yabuki and Matsu'ura 1992; Fukahata et al. 1996; Okazaki et al. 2021).

We express the velocity field $v(x)$ as a linear combination of a set of basis functions $\{\phi_k(x)\}_{k=1}^{M}$:

$$v(x) = \sum_{k=1}^{M} a_k \phi_k(x), \tag{4}$$

where a_k is a model parameter to be estimated from observed data and M is the number of model parameters. Using the model velocity field (Eq. 4) and observed velocities (Eq. 3), we obtain the following observation equation:

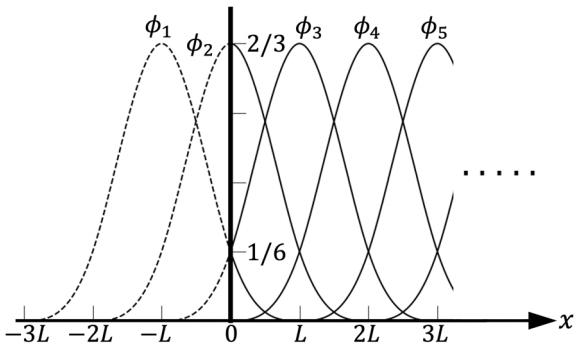

Fig. 3 Functional form of cubic B-splines, which are used as basis functions in this analysis. At the boundaries of the model region, the cubic B-splines are truncated

$$\mathbf{d} = \mathbf{H}\mathbf{a} + \mathbf{e}, \tag{5}$$

where $\mathbf{a} = (a_1, \ldots, a_M)^{\mathrm{T}}$, is the model parameter vector, and $\mathbf{e}$ is the residual between the model and observed velocities; $\mathbf{e}$ is assumed to follow a Gaussian distribution $\mathbf{e} \sim N(0, \sigma_e^2 \mathbf{I})$, where σ_e^2 is an unknown scale of errors and $\mathbf{I}$ is the $N \times N$ unit matrix. The matrix $\mathbf{H}$ is expressed by the values of ϕ_k as:

$$\mathbf{H} \equiv \begin{pmatrix} \phi_1(x_1) & \cdots & \phi_M(x_1) \\ \vdots & \ddots & \vdots \\ \phi_1(x_N) & \cdots & \phi_M(x_N) \end{pmatrix}. \tag{6}$$

Cubic B-splines, defined below, are used as the basis functions (de Boor 1972; Cox 1972; Yabuki and Matsu'ura 1992):

$$\phi_k(x) = \frac{1}{6L^3} \times \begin{cases} (x - x_k + 2L)^3, & x_k - 2L \le x \le x_k - L \\ -3(x - x_k)^3 - 6L(x - x_k)^2 + 4L^3, & x_k - L \le x \le x_k \\ 3(x - x_k)^3 - 6L(x - x_k)^2 + 4L^3, & x_k \le x \le x_k + L \\ -(x - x_k - 2L)^3, & x_k + L \le x \le x_k + 2L \\ 0, & x < x_k - 2L \text{ or } x_k + 2L < x \end{cases} \tag{7}$$

with

$$x_k = x_{\min} + (k-2)L,\ k = 1, 2, \ldots, K+3, \tag{8}$$

$$K = \frac{x_{\max} - x_{\min}}{L}, \tag{9}$$

where L is the interval of basis functions (Fig. 3), M equals to $K+3$, and $[x_{\min}, x_{\max}]$ corresponds to the model region. Following Okazaki et al. (2021), the basis functions are truncated at the boundaries of the model region (Fig. 3).

Under the assumption that velocity fields should change smoothly in space, we impose smoothness constraint as the prior constraint, which is expressed by the L2-norm of the second derivatives of the velocity field. The objective function for the L2 regularization is expressed as:

$$\begin{aligned} s(\mathbf{a}; \beta) &= (\mathbf{d} - \mathbf{H}\mathbf{a})^{\mathrm{T}}(\mathbf{d} - \mathbf{H}\mathbf{a}) + \beta \mathbf{a}^{\mathrm{T}}\mathbf{R}\mathbf{a} \\ &= (\mathbf{d} - \mathbf{H}\mathbf{a})^{\mathrm{T}}(\mathbf{d} - \mathbf{H}\mathbf{a}) + \beta \|\mathbf{H}_{xx}\mathbf{a}\|_2^2, \end{aligned} \tag{10}$$

where the matrix $\mathbf{H}_{xx}$ is composed of the second derivatives of the basis functions as:

$$\mathbf{H}_{xx} \equiv \begin{pmatrix} \phi_1^{xx}(x_1) & \cdots & \phi_M^{xx}(x_1) \\ \vdots & \ddots & \vdots \\ \phi_1^{xx}(x_N) & \cdots & \phi_M^{xx}(x_N) \end{pmatrix}, \tag{11}$$

with

$$\begin{aligned} \phi_k^{xx}(x) &\equiv \frac{\partial^2 \phi_k}{\partial x^2}(x) \\ &= \frac{1}{L^3} \times \begin{cases} x - x_k + 2L, & x_k - 2L \le x \le x_k - L \\ -3(x - x_k) - 2L, & x_k - L \le x \le x_k \\ 3(x - x_k) - 2L, & x_k \le x \le x_k + L \\ -(x - x_k - 2L), & x_k + L \le x \le x_k + 2L \\ 0, & x < x_k - 2L \text{ or } x_k + 2L < x \end{cases} \end{aligned} \tag{12}$$

The first term of the right-hand side of Eq. (10) represents the residual sum of squares (RSS) between the estimated and observed velocities and the second term represents the smoothness constraint. The explicit expression of $\mathbf{R}$ is given in the Appendix of Nozue and Fukahata (2022). β is a hyperparameter that controls the weight of the smoothness constraint relative to the RSS. Given β, the model parameter is obtained by minimizing Eq. (10) as:

$$\hat{\mathbf{a}} = \left(\mathbf{H}^{\mathrm{T}}\mathbf{H} + \beta\mathbf{R}\right)^{-1}\mathbf{H}^{\mathrm{T}}\mathbf{d}. \tag{13}$$

The optimal value of β can be objectively determined by minimizing ABIC (Akaike 1980). In this case, ABIC is expressed as follows (Yabuki and Matsu'ura 1992; Okazaki et al. 2021):

$$\begin{aligned} \mathrm{ABIC}(\beta) = &\ (N + P - M)\log s(\mathbf{a}; \beta) \\ &- P\log\beta + \log\left|\mathbf{H}^{\mathrm{T}}\mathbf{H} + \beta\mathbf{R}\right| + C, \end{aligned} \tag{14}$$

where P is the rank of $\mathbf{R}$. Substituting the optimal value of β into Eq. (13), the optimal model parameters are obtained.

2.3 Introduction of sparse modeling

Next, we explain the new method to estimate a strain-rate field introducing sparse modeling. Considering that a strain-rate field is smooth in most areas, but can change abruptly in a narrow zone such as a fault zone, we apply both the sparsity constraint and the smoothness constraint on strain rates, which are expressed by the L1-norm and the L2-norm of the second derivatives of the velocity field, respectively. Then, the objective function to be minimized is expressed as:

$$E(\mathbf{a};\alpha,\beta) = (\mathbf{d}-\mathbf{Ha})^{\mathrm{T}}(\mathbf{d}-\mathbf{Ha}) + \alpha\|\mathbf{H}_{xx}\mathbf{a}\|_1 + \beta\|\mathbf{H}_{xx}\mathbf{a}\|_2^2 \tag{15}$$

where $\|\mathbf{H}_{xx}\mathbf{a}\|_1$ and $\|\mathbf{H}_{xx}\mathbf{a}\|_2$ are the L1-norm and the L2-norm of $\mathbf{H}_{xx}\mathbf{a}$, respectively. α and β are the hyperparameters that control the weights of the sparsity constraint and the smoothness constraint relative to the RSS, respectively. Since we consider an anti-plane strain problem, Eq. (15) can be written as:

$$E(\mathbf{a};\alpha,\beta) = \sum_{i=1}^{N}\left(v_i - \sum_{j=1}^{M} H_{ij}a_j\right)^2 + \alpha\int\left|\sum_{j=1}^{M} a_j\frac{\mathrm{d}^2\phi_j}{\mathrm{d}x^2}(x)\right|\mathrm{d}x + \beta\int\left\{\sum_{j=1}^{M} a_j\frac{\mathrm{d}^2\phi_j}{\mathrm{d}x^2}(x)\right\}^2\mathrm{d}x. \tag{16}$$

To determine the optimal values of the hyperparameters $(\alpha,\beta) = \left(\widehat{\alpha},\widehat{\beta}\right)$, we use the method of leave-one-out cross-validation (LOOCV) (e.g., Stone 1974; Geisser 1975). For fixed values of (α,β) and the velocity data at $N-1$ observation points, where the data at the n-th observation point $(x = x_n)$ is excluded, the objective function is defined as:

$$E_n(\mathbf{a};\alpha,\beta) = \sum_{i\neq n}^{N}\left(v_i - \sum_{j=1}^{M} H_{ij}a_j\right)^2 + \alpha\int\left|\sum_{j=1}^{M} a_j\frac{\mathrm{d}^2\phi_j}{\mathrm{d}x^2}(x)\right|\mathrm{d}x + \beta\int\left\{\sum_{j=1}^{M} a_j\frac{\mathrm{d}^2\phi_j}{\mathrm{d}x^2}(x)\right\}^2\mathrm{d}x. \tag{17}$$

Here, the solution of model parameter vector $\mathbf{a}^n$ that minimizes $E_n(\mathbf{a};\alpha,\beta)$ is obtained by the Broyden–Fletcher–Goldfarb–Shanno (BFGS) method described later. Using $\mathbf{a}^n$, we compute the squared residual r_n between the observed and the calculated velocities at $x = x_n$. We calculate r_n for all n (1,2, . . . , N), and sum up them to obtain the evaluation function of LOOCV:

$$r(\alpha,\beta) \equiv \sum_{n=1}^{N} r_n = \sum_{n=1}^{N}\left(v_n - \sum_{j=1}^{M} H_{nj}a_j^n\right)^2. \tag{18}$$

In minimizing $E(\mathbf{a};\alpha,\beta)$ and $E_n(\mathbf{a};\alpha,\beta)$, we use the BFGS method (Broyden 1970; Fletcher 1970; Goldfarb 1970; Shanno 1970), which is one type of quasi-Newton method: an algorithm to find the minimum point of objective functions in nonlinear optimization problems. The descent direction for unknown parameters is determined by the approximation to the Hessian matrix, which is generated by the second derivatives of the objective function. Unknowns are updated in the descent direction and then a new approximate matrix of the Hessian is calculated. This calculation is repeated until the gradient of the objective function becomes sufficiently small. However, since the problem is nonlinear, obtained solutions may differ depending on the initial values of model parameters. In this study, for simplicity, the zero vector is used as the initial values of model parameters.

3 Synthetic tests

3.1 Setting of synthetic tests

To confirm the validity and limitations of the proposed method, we conduct numerical experiments on the anti-plane problem, explained in Sect. 2.1 and Fig. 2. We set the model area from −80 km to 80 km along the x-axis. Because the basis functions (cubic B-splines; Eq. 7) are placed with the interval of $L = 5$ km and truncated at the edge of the profile (Fig. 3), the number of basis functions is $M = 35$.

In the following, we calculate $r(\alpha,\beta)$ by changing the values of the hyperparameters within the ranges of $10^{-4} \le \alpha \le 10^2$ and $10^0 \le \beta \le 10^4$ with $10^{0.25}$ grid spacing both for α and β (e.g., Figure S1). Here, the problem is how to determine the optimal pair of the hyperparameter values. Smaller $r(\alpha,\beta)$ generally gives a better pair of the hyperparameters. However, it should be noticed that the global minimum of $r(\alpha,\beta)$ does not always give the optimal solution, because Eq. (15) is a nonlinear equation. For example, Sato et al. (2022) showed that maximum a posteriori (MAP) of the joint posterior probability of the hyperparameters and model parameters often gives an inappropriate solution; instead, the minimum of ABIC, which is calculated by the integration of the joint posterior probability with respect to the model parameters, gives the optimal solution. This means that an operation taking an average is effective in obtaining an appropriate solution. Therefore, in this study, we apply a moving average filter to $r(\alpha,\beta)$ in obtaining the optimal pair of hyperparameters. Specifically, we calculate the average value of $r(\alpha,\beta)$ for the pairs of hyperparameters $\left(\alpha',\beta'\right)$ within the

Table 1 List of parameters for synthetic tests and optimal values of the hyperparameters

D(km)	A(km)	σ (mm/yr)	$\log_{10}\widehat{\alpha}$	$\log_{10}\widehat{\beta}$	$\log_{10}\widehat{\beta}_{L2}$
5	10	0.0	−2.00	0.75	1.75
	20		−1.25	2.50	3.50
10	10		−3.25	0.75	−5.00
	20		−3.25	1.75	2.75
20	10		−3.25	0.75	−5.00
	20		−3.25	1.50	−5.00
10	10	0.1	0.00	2.00	2.25
		0.2	0.25	2.25	2.50
		0.4	0.25	2.75	3.25

The values of the hyperparameters $(\widehat{\alpha},\widehat{\beta})$ for the proposed method and $\widehat{\beta}_{L2}$ for the L2 regularization method are shown. D: locking depth, A: observation interval, σ: observation error

range of $\left|\log_{10}\alpha-\log_{10}\alpha'\right|+\left|\log_{10}\beta-\log_{10}\beta'\right|\leq 0.75$, and determine the optimal pair of the hyperparameters $\left(\widehat{\alpha},\widehat{\beta}\right)$ that minimizes this average value. Once we obtain the optimal hyperparameters $\left(\widehat{\alpha},\widehat{\beta}\right)$ (Figures S1-S3), we can estimate the optimal model parameters $\widehat{\mathbf{a}}$ by minimizing $E\left(\mathbf{a};\widehat{\alpha},\widehat{\beta}\right)$. By substituting $\widehat{\mathbf{a}}$ into Eq. (4), the velocity profile is obtained, and by differentiating it with respect to x, the strain-rate profile is also obtained.

In the synthetic tests, we change the parameters D, A, and σ to generate the velocity data, while fixing the steady slip rate and the spatial velocity gradient to $s = 5$ mm/yr and $\mu = 1.0\times10^{-8}$/yr, respectively. Table 1 summarizes the list of parameters for synthetic tests with the optimal values of the hyperparameters (Figures S1–S3).

3.2 Dependence on the locking depth

We compare the results for the cases with different values of locking depth D =5 km, 10 km, and 20 km (Fig. 4), while observation interval A and observation error σ are fixed to 10 km and 0 mm/yr, respectively. As shown in Eq. (2), a smaller value of D results in a narrower strain concentration zone. In the case of $D = 5$ km, the peak

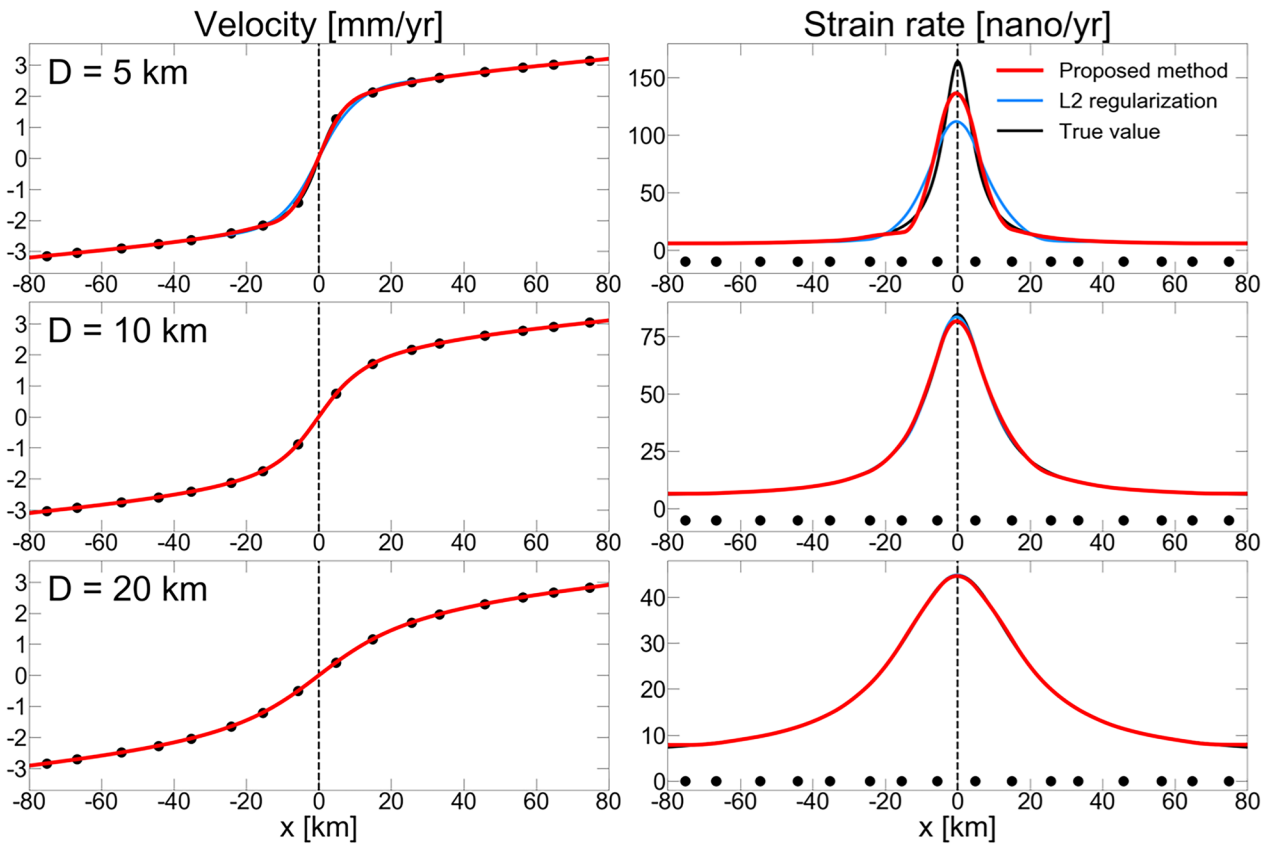

Fig. 4 Dependence of the estimated velocity (left) and strain-rate (right) profiles on the locking depth D of 5 km (top), 10 km (middle), and 20 km (bottom). Results of the proposed method and the L2 regularization method, and the true profiles are shown by the red, blue, and black lines, respectively. Observed velocities (left) and observation points (right) are also plotted by the small black circles. The observation interval A and the observation error σ are fixed to 10 km and 0 mm/yr, respectively

strain rate estimated by the proposed method is about 20% larger than that by the L2 regularization, although it is still about 20% smaller than the true one. The estimation accuracy near the fault is clearly improved by the proposed method. On the other hand, for $D=10$ km and 20 km, in which the strain concentration near the fault is weaker, both the proposed method and the L2 regularization method reproduce the peak strain rates almost perfectly, although the latter is slightly (a few percents) better in the recovery ratio of the true peak value (Figure S4). In brief, the proposed method achieves almost equivalent or higher accuracy than the L2 regularization method, whether the strain concentration zone is wide or narrow.

3.3 Dependence on the observation interval

We compare the strain-rate profiles for the cases with $A=10$ km and 20 km, while D is changed to 5 km, 10 km, and 20 km with $\sigma = 0$ mm/yr (Fig. 5). In general, fewer observation points result in a larger weight of the prior constraint in the objective function. When $A=10$ km, the proposed method estimates the peak strain rate larger than the L2 regularization method for the case of $D=5$ km, while both methods estimate almost the same peak values for the cases of $D=10$ km and 20 km as described in Sect. 3.2. On the other hand, when $A=20$ km, the proposed method estimates larger peak strain rates than the L2 regularization method for the cases not only for $D=5$ km but also for $D=10$ km. This suggests that the proposed method shows higher performance than the L2 regularization under the worse condition that fewer observation points are available. For reference, we investigate the cases with different values of D (5 km–20 km) (Figure S4). The superiority of the proposed method against the L2 regularization method is clearer for $A=20$ km than for $A=10$ km, although the L2 regularization method shows slightly better performance than the proposed method for the cases of larger D. In brief, the proposed method shows better performance when the data coverage is worse (larger A) and the strain concentration zone is narrower (smaller D).

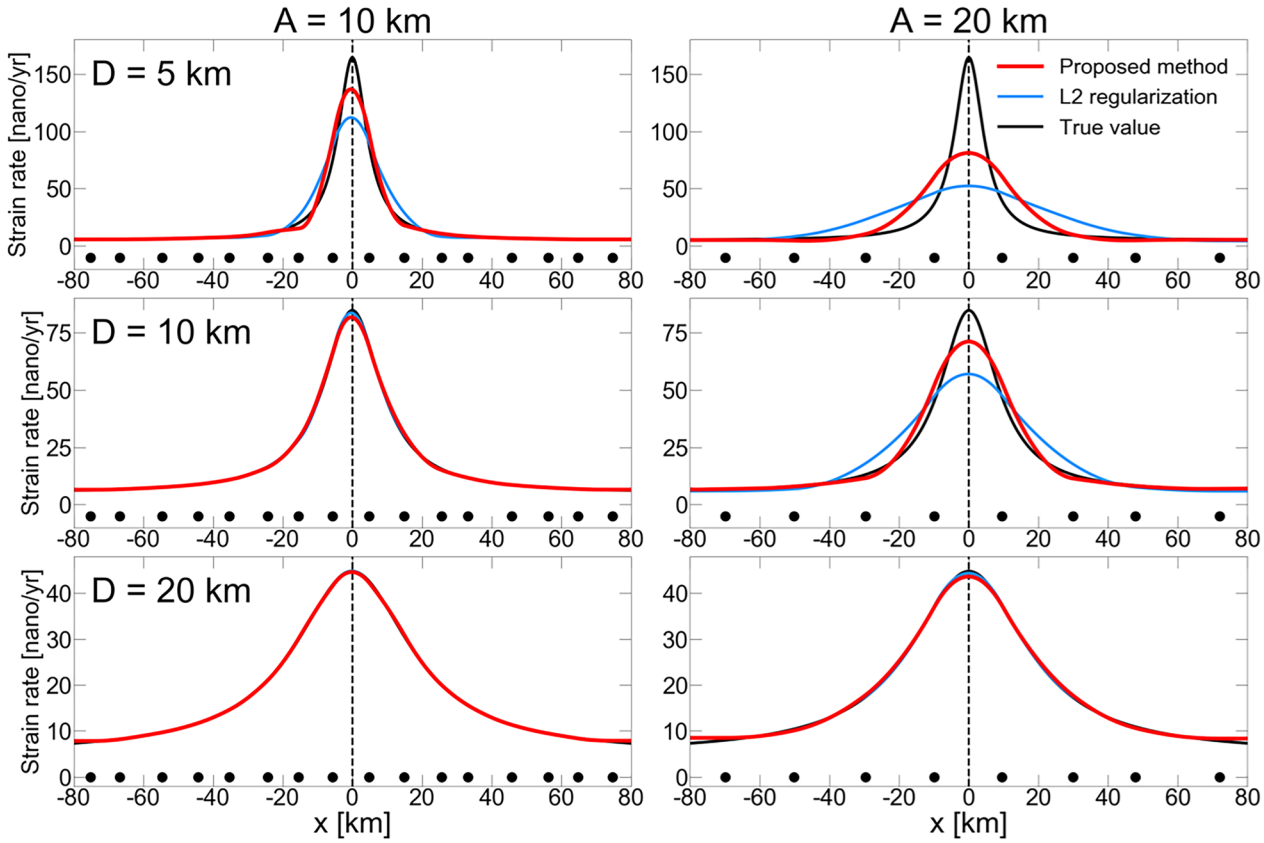

Fig. 5 Dependence of the estimated strain-rate profiles on the observation interval A of 10 km (left) and 20 km (right), where the locking depth D is also changed to 5 km (top), 10 km (middle), and 20 km (bottom). Results of the proposed method and the L2 regularization method, and the true profiles are shown by the red, blue, and black lines, respectively. Locations of observation points are also plotted. The observation error σ is fixed to 0 mm/yr. The left column of this figure is the same as the right column of Fig. 4

3.4 Dependence on observation errors

We compare the profiles for the cases with $\sigma = 0.1$ mm/yr, 0.2 mm/yr, and 0.4 mm/yr, while fixing $D = 10$ km and $A = 10$ km (Fig. 6). For the cases of $\sigma = 0.1$ mm/yr and 0.2 mm/yr, the proposed method estimates almost the same values of the strain rates near the fault as the L2 regularization method does. However, the strain-rate profiles estimated by the proposed method show smaller variations far from the fault than those by the L2 regularization method. On the other hand, for the case of $\sigma = 0.4$ mm/yr, both methods estimate the strain-rate profiles quite different from the true profiles, particularly for the range of $x \leq -50$ km. In summary, the proposed method is applicable effectively if observation errors are small.

4 Application to Arima-Takatsuki fault zone

4.1 GNSS data and analysis domain

We apply the proposed method to GNSS velocity data across the Arima-Takatsuki fault zone (ATFZ), and compare the results by the L2 regularization method. ATFZ, which is located in central Japan, is a group of right-lateral strike-slip faults (Fig. 7). ATFZ is one of the most active strike-slip faults in Japan. In the eastern part of this fault zone, at least 3 large inland earthquakes have occurred in the last 3000 years: about B.C. 1000, A.D. 700–1300, and 1596 (e.g., The Headquarters for Earthquake Research Promotion 2001). The fault slip of each earthquake was estimated at up to 3 m. Because this fault zone is located inland, we can take a relatively long profile and use many observation stations. Therefore, we apply the proposed method to GNSS data across this fault zone.

The active faults composing ATFZ generally have a strike of N70°–80° E with a dip of about 90° (e.g., The Geological Survey of Japan, National Institute of Advanced Industrial Science and Technology 2023). As shown in Fig. 7, we take the x-axis (blue line) perpendicular to ATFZ (red line). The origin of the x-axis, (135.42° E, 34.83° N), is the intersection of the blue and red lines. The x-axis is oriented to N10° W with the positive direction southward.

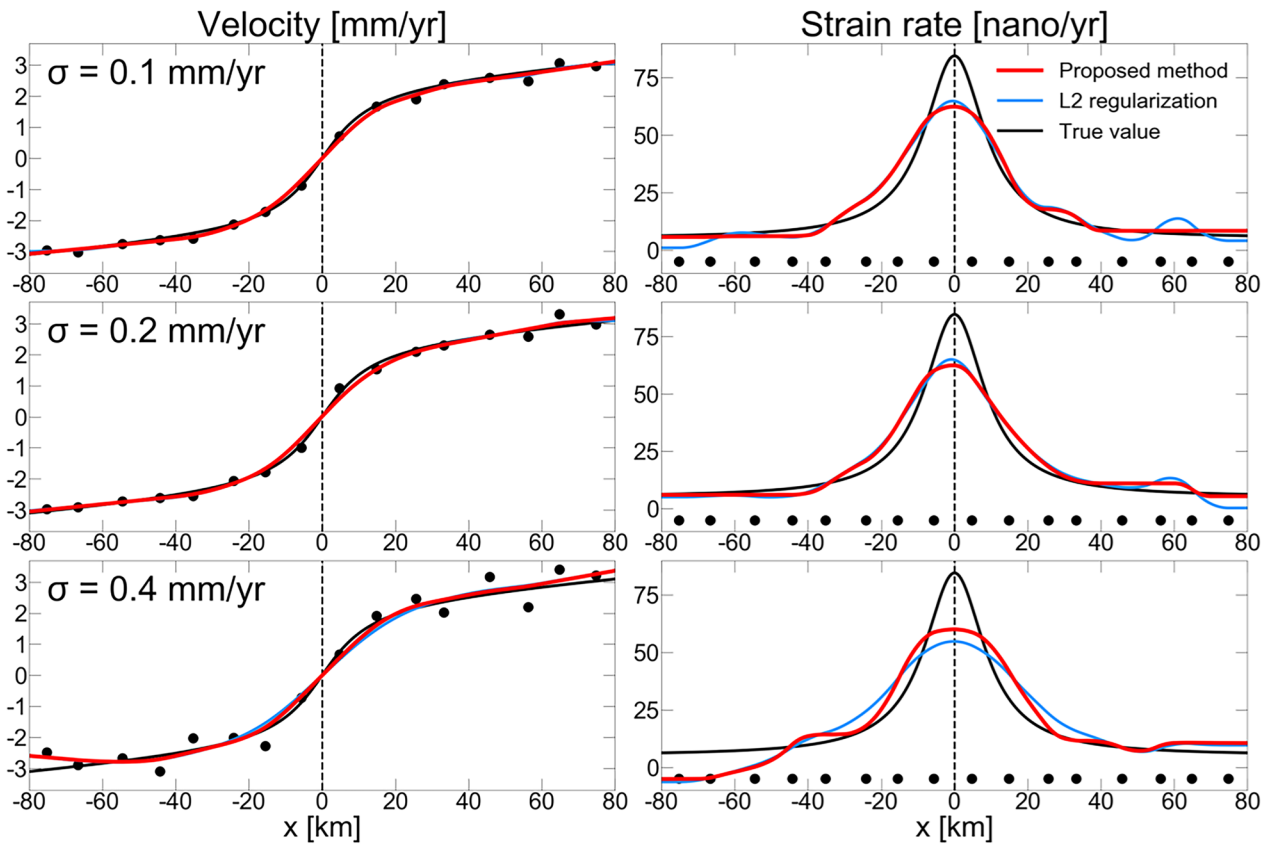

Fig. 6 Dependence of the estimated velocity (left) and strain-rate profiles (right) on the observation error σ of 0.1 mm/yr (top), 0.2 mm/yr (middle), and 0.4 mm/yr (bottom). Results of the proposed method and the L2 regularization method, and the true profiles are shown by the red, blue, and black lines, respectively. Observed velocities (left) and observation points (right) are also plotted. Both the observation interval A and the locking depth D are fixed to 10 km

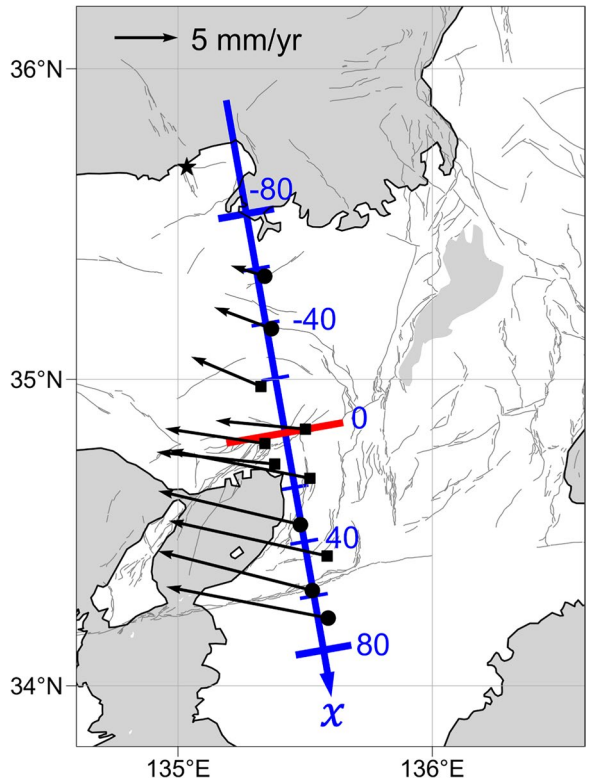

Fig. 7 Horizontal velocities at GEONET stations across the Arima-Takatsuki fault zone used in this study. The velocities are shown with respect to the reference point ('960640'; black star). The *x*-axis (blue line) is taken to be perpendicular to the strike of the Arima-Takatsuki fault zone (red line), the location of which is taken to be $x = 0$. GEONET stations within 5 km (circles) and 5–10 km (squares) from the *x*-axis are shown. Active faults are shown by gray lines

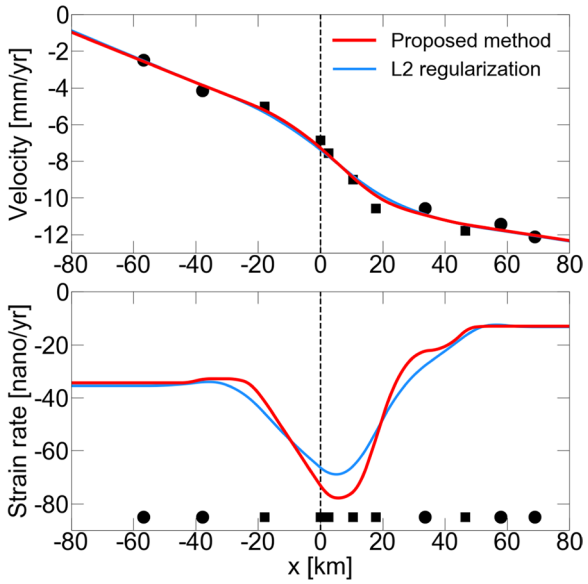

Fig. 8 Estimated velocity profile (top) and strain-rate profile (bottom) across the Arima-Takatsuki fault zone. The results of the proposed method (red) and the L2 regularization method (blue) are presented. The locations of observation points within 5 km (circles) and 5–10 km (squares) from the *x*-axis are also shown

Along the x-axis from $x = -80$ km to $x = 80$ km, there are 11 GNSS stations operated by the GSI within 10 km from the x-axis (Fig. 7). For these stations, we estimated average velocities in the fault-perpendicular direction by the following method: (1) we obtained the daily coordinates of the F5 solution (Takamatsu et al. 2023), based on the International Terrestrial Reference Frame (ITRF) 2014 (Altamimi et al. 2016). The data used in the analysis spans from January 2001 to December 2010, except for the data at one station where data are available from March 2003 due to the timing of its installation. The end of the data period was set to avoid the effect of the 2011 Tohoku-oki earthquake. (2) Following the procedure of Sagiya et al. (2000), the obtained daily coordinates at each station are fitted by the least-square method with the functions of a linear trend, annual and semiannual sinusoidal components, and coordinate offsets due to large earthquakes ($M_j \geq 6.0$) and the equipment maintenance (Figure S5), and then the coefficient of the linear trend is used as the velocity component (black vectors in Fig. 7). Here, M_j stands for the magnitude determined by the Japan Meteorological Agency (JMA). The standard deviation of observation errors, evaluated by the procedure of Dixon et al. (2000), is less than 0.2 mm/yr at every station, reflecting a relatively long observation period. Since we consider the anti-plane strain problem, each observation point is projected onto the x-axis, and the fault parallel velocity is used in the analysis.

4.2 Results

Applying the proposed method to GNSS data, we estimate the strain rate across ATFZ, and compare the result by the L2 regularization method. The distribution of the values of $r(\alpha, \beta)$, calculated by the LOOCV procedure, is shown in Figure S6 together with the ABIC curve for the L2 regularization method. The optimal values of the hyperparameters are $\widehat{\alpha} = 10^{0.25}, \widehat{\beta} = 10^{2.75}$ for the proposed method and $\widehat{\beta} = 10^{3.25}$ for the L2 regularization method. Using these values, we estimate the velocity and strain-rate profiles. The location of the peak strain rate is almost the same for both methods. As expected from the synthetic tests, however, we obtain a sharper peak of strain rates by the proposed method than by the L2 regularization method. The estimated peak strain rate is

78×10^{-9}/yr for the proposed method and 69×10^{-9}/yr for the L2 regularization method; the difference is about 10×10^{-9}/yr (Fig. 8). Since the strain rates in the surrounding area are 35×10^{-9}/yr ($x = -80$ km) and 13×10^{-9}/yr ($x = 80$ km), the increase of the strain rate around the fault zone from the surrounding area is about 20–30% larger by the proposed method than by the L2 regularization method. This example indicates that the proposed method works well in estimating localized high strain rates.

From the obtained strain-rate profiles, we estimate the locking depth D and the steady slip rate s of the fault by fitting to the crustal deformation model expressed by Eq. (2), though it is slightly modified to:

$$\dot{e}(x) = \frac{1}{2}\frac{\mathrm{d}v}{\mathrm{d}x} = \frac{sD}{2\pi}\frac{1}{(x - x_{\mathrm{peak}})^2 + D^2} + \frac{\mu}{2}, \qquad (19)$$

where x_{peak} is the location of the peak strain rate. For simplicity, we fix μ to 5.0×10^{-8}/yr, near the average value of the strain rates at $x = -80$ km and $x = 80$ km, and x_{peak} to 5.8 km for the proposed method and 5.2 km for the L2 regularization method, respectively. By minimizing the value of RSS between the estimated strain rates and analytical values (Eq. 19) in the range of $x_{\mathrm{peak}} - 40 \le x \le x_{\mathrm{peak}} + 40$ km, we obtain the optimal values of D and s as 11 km and 4 mm/yr for the proposed method, while 17 km and 5 mm/yr for the L2 regularization. The steady slip rate estimated by the proposed method is realistic; the slip of 4 mm/yr reaches 3 m, the coseismic slip in each large earthquake, in about 800 years, which is comparable to the intervals of historical earthquakes (The Headquarters for Earthquake Research Promotion 2001). According to seismological studies (e.g., Ito and Nakamura 1998; Omuralieva et al. 2012), D90, above which 90% of earthquakes occur, is 12–14 km around ATFZ. This suggests that the proposed method estimates a more realistic locking depth than the L2 regularization.

5 Discussion and conclusions

It has been difficult to accurately estimate localized strain rates around a fault zone from GNSS data. To overcome this difficulty, we newly introduced sparse modeling. By using the objective function with the L1-norm and the L2-norm regularization terms, we imposed both the sparsity constraint and the smoothness constraint on strain rates as prior information.

In synthetic tests, we considered an anti-plane strain problem due to a steady slip on a buried strike-slip fault, for simplicity. As a result, we found the following: (1) the proposed method shows almost equal or better performance than the L2 regularization method regardless of the locking depth (Fig. 4). (2) The advantage of the proposed method over the L2 regularization method becomes clearer under the worse condition that fewer observation points are available (Fig. 5). In brief, the proposed method shows better performance when the data coverage is worse and the strain concentration zone is narrower.

We also found (3) the proposed method is applicable if observation errors of velocity data are small, but it does not work well for cases with large errors (Fig. 6). Of course, the acceptable error level depends on the magnitude of the signal; for faster strain-rate concentration, larger errors are acceptable. The noise sensitive behavior of the proposed method is probably due to a famous trade-off between the model resolution and accuracy in inversion analyses (Backus and Gilbert 1970). Because the proposed method enhances the resolution of a strain-rate field, estimation errors tend to be larger.

The proposed method was applied to GNSS velocity data across ATFZ. The proposed method estimates about 20–30% larger value of the increase of the strain rate around the fault zone from the surrounding area than the L2 regularization method (Fig. 8). Additionally, a more realistic locking depth is estimated by the proposed method than by the L2 regularization.

It should be noted that the proposed method is developed to detect strain-rate concentration. In other words, the method can be applicable, even if the strain-rate profile does not follow an arctangent model in the anti-plane strain problem (Eq. 3). For example, the strain-rate profile estimated by the proposed method deviates from the arctangent model (Fig. 8), although we fitted an arctangent model to it for easy comprehension.

As shown in this paper, the proposed method exhibits a high performance in estimating localized strain rates. However, since the velocity component perpendicular to the fault strike is ignored, the effectiveness of the method is limited. In the future, we plan to extend the proposed method to two-dimensional cases. Through this improvement, it is expected we can obtain strain-rate fields more precisely, which will lead to useful knowledge for probabilistic forecasts of earthquakes and understanding of the development of geological structures.

Abbreviations

ABIC	Akaike's Bayesian Information Criterion
ATFZ	Arima-Takatsuki fault zone
BFGS	Broyden–Fletcher–Goldfarb–Shanno
DDC	Distance Decaying Constant
GEONET	GNSS Earth Observation Network System
GNSS	Global Navigation Satellite System
GSI	Geospatial Information Authority of Japan

ITRF	International Terrestrial Reference Frame
JMA	Japan Meteorological Agency
LASSO	Least absolute shrinkage and selection operator
LOOCV	Leave-one-out cross-validation
MAP	Maximum a posteriori
NKTZ	Niigata-Kobe Tectonic Zone
RSS	Residual sum of squares

Supplementary Information

The online version contains supplementary material available at https://doi.org/10.1186/s40623-024-02115-3.

Supplementary Material 1.

Acknowledgements
GNSS data were obtained from the Geospatial Information Authority of Japan (GSI). We thank Dr. Bogdan Enescu and two anonymous reviewers for useful comments, which contributed to improving the manuscript

Author contributions
YN and YF designed this study. YN carried out the analysis of velocity and strain-rate fields. Both authors discussed the results and prepared the manuscript.

Funding
This work was supported by JSPS KAKENHI No. 23KJ1371 to YN and No. 22K03759 to YF and the grant provided by the Iwadare Scholarship Foundation to YN.

Availability of data and materials
The GNSS displacement data we used can be downloaded from the GSI website.

Declarations

Consent for publication
Not applicable.

Competing interests
Both authors declare that they have no competing interests.

Author details
[1]Division of Earth and Planetary Sciences, Graduate School of Science, Kyoto University, Gokasho, Uji, Kyoto 611-0011, Japan. [2]Disaster Prevention Research Institute, Kyoto University, Gokasho, Uji, Kyoto 611-0011, Japan.

Received: 23 April 2024 Accepted: 4 December 2024
Published online: 03 February 2025

References

Akaike H (1980) Likelihood and the Bayes procedure. In: Bernardo JM, DeGroot MH, Lindley DV, Smith AFM (eds) Bayesian statistics. University Press, Valencia, pp 143–166. https://doi.org/10.1007/BF02888350
Altamimi Z, Rebischung P, Metivier L, Collilieux X (2016) ITRF2014: a new release of the International Terrestrial Reference Frame modeling nonlinear station motions. J Geophys Res Solid Earth 121(8):6109–6131. https://doi.org/10.1002/2016JB013098
Backus G, Gilbert F (1970) Uniqueness in the inversion of inaccurate gross Earth data. Phil Transact Royal Soc London Series a, Math Phys Sci 266:123–192. https://doi.org/10.1098/rsta.1970.0005
Bird P (2003) An updated digital model of plate boundaries. Geochem Geophys Geosyst. https://doi.org/10.1029/2001GC000252
Broyden CG (1970) The convergence of a class of double-rank minimization algorithms: 2. The new algorithm. IMA J Appl Math 6(3):222–231. https://doi.org/10.1093/imamat/6.3.222
Cox MG (1972) The numerical evaluation of B-splines. IMA J Appl Math 10(2):134–149. https://doi.org/10.1093/imamat/10.2.134
de Boor C (1972) On calculating with B-splines. J Approx Theory 6(1):50–62. https://doi.org/10.1016/0021-9045(72)90080-9
Dixon TH, Miller M, Farina F, Wang H, Johnson D (2000) Present-day motion of the Sierra Nevada block and some tectonic implications for the Basin and Range Province, North American Cordillera. Tectonics 19(1):1–24. https://doi.org/10.1029/1998TC001088
Evans EL, Meade BJ (2012) Geodetic imaging of coseismic slip and postseismic afterslip: Sparsity promoting methods applied to the great Tohoku earthquake. Geophys Res Lett 39(11):L11314. https://doi.org/10.1029/2012GL051990
Fletcher R (1970) A new approach to variable metric algorithms. Comput J 13(3):317–322. https://doi.org/10.1093/comjnl/13.3.317
Fukahata Y, Honsho C, Matsu'ura M (1996) Crustal movements on Shikoku, southwestern Japan, inferred from inversion analysis of levelling data using ABIC. Tectonophysics 257(2–4):239–252. https://doi.org/10.1016/0040-1951(95)00176-X
Fukahata Y, MenesesGutierrez A, Sagiya T (2020) Detection of plastic strain using GNSS data of pre- and post-seismic deformation of the 2011 Tohoku-oki earthquake. Earth Planets Space 72:18. https://doi.org/10.1186/s40623-020-1144-1
Fukahata Y, Okazaki T, Nishimura T (2022) Strain-rate field of Japan estimated from GNSS data and its interpretation based on inter- and intra-arc deformation. J Geogr 131(5):479–496. https://doi.org/10.5026/jgeography.131.479
Geisser S (1975) The predictive sample reuse method with applications. J Am Stat Asso 70(350):320–328. https://doi.org/10.2307/2285815
Goldfarb D (1970) A family of variable-metric methods derived by variational means. Math Comp 24:23–26. https://doi.org/10.2307/2004873
Hori T, Nakata R, Hino H, Kuwatani T, Yoshioka S, Okada M (2018) Geodetic inversion for spatial distribution of slow earthquakes under sparsity constraints. In: Paper presented at the International Meeting on "High-Dimensional Data-Driven Science" (HD3–2017), Kyoto, 10–13 Sep 2017. https://doi.org/10.1088/1742-6596/1036/1/012018
Huzita K (1980) Role of the median tectonic line in the Quaternary tectonics of Japanese islands. Mem Geol Soc Japan 18:129–153
Ito K, Nakamura S (1998) Variations in thickness of the seismogenic layer in southwestern Japan and their relation to large inland earthquakes. Annu Disas Prev Res Inst Kyoto Univ 41(B-1):27–35 (in Japanese with English abstract)
Lustig M, Donoho D, Pauly JM (2007) Sparse MRI: The application of compressed sensing for rapid MR imaging. Magn Reson Med 58(6):1182–1195. https://doi.org/10.1002/mrm.21391
Matsu'ura M, Jackson DD, Cheng A (1986) Dislocation model for aseismic crustal deformation at Hollister, California. J Geophys Res 91(12):12661–12674. https://doi.org/10.1029/JB091iB12p12661
Meneses-Gutierrez A, Sagiya T (2016) Persistent inelastic deformation in central Japan revealed by GPS observation before and after the Tohoku-oki earthquake. Earth Planet Sci Lett 450(15):366–371. https://doi.org/10.1016/j.epsl.2016.06.055
Nakata R, Kuwatani T, Okada M, Hori T (2016) Geodetic inversion for spatial distribution of slip under smoothness, discontinuity, and sparsity constraints. Earth Planets Space 68:20. https://doi.org/10.1186/s40623-016-0396-2
Nakata R, Hino H, Kuwatani T, Yoshioka S, Okada M, Hori T (2017) Discontinuous boundaries of slow slip events beneath the Bungo Channel, southwest Japan. Sci Rep 7:6129. https://doi.org/10.1038/s41598-017-06185-0
Nishimura T (2017) Strain concentration zones in the Japanese Islands clarified from GNSS data and its relation with active faults and inland earthquakes. Active Fault Res 46:33–39. https://doi.org/10.11462/afr.2017.46_33
Nishimura T (2022) Time-independent forecast model for large crustal earthquakes in southwest Japan using GNSS data. Earth Planets Space 74:58. https://doi.org/10.1186/s40623-022-01622-5
Nishimura T, Yokota Y, Tadokoro K, Ochi T (2018) Strain partitioning and interpolate coupling along the northern margin of the Philippine Sea plate, estimated from Global Navigation Satellite System and Global Positioning System-Acoustic data. Geosphere 14(2):535–551. https://doi.org/10.1130/GES01529.1
Nozue Y, Fukahata Y (2022) Comparison between the boxcar and cubic B-spline functions in estimating displacement fields by basis function

expansion. J Seismol Soc Japan 2(75):1–12. https://doi.org/10.4294/zisin.2021-8. (in Japanese with English abstract)
Okazaki T, Fukahata Y, Nishimura T (2021) Consistent estimation of strain-rate fields from GNSS velocity data using basis function expansion with ABIC. Earth Planets Space 73:153. https://doi.org/10.1186/s40623-021-01474-5
Okuwaki R, Yagi Y, Murakami A, Fukahata Y (2024) A multiplex rupture sequence under complex fault network due to preceding earthquake swarms during the 2024 Mw 7.5 Noto Peninsula, Japan, Earthquake. Geophys Res Lett 51(11):e2024GL109224. https://doi.org/10.1029/2024GL109224
Omuralieva AM, Hasegawa A, Matsuzawa T, Nakajima J, Okada T (2012) Lateral variation of the cutoff depth of shallow earthquakes beneath the Japan Islands and its implications for seismogenesis. Tectonophysics 518–521:93–105. https://doi.org/10.1016/j.tecto.2011.11.013
Sagiya T, Miyazaki S, Tada T (2000) Continuous GPS array and present-day crustal deformation of Japan. Pure Appl Geophys 157:2303–2322. https://doi.org/10.1007/PL00022507
Sato DSK, Fukahata Y, Nozue Y (2022) Appropriate reduction of the posterior distribution in fully Bayesian inversions. Geophys J Int 231(2):950–981. https://doi.org/10.1093/gji/ggac231
Savage JC, Burford RO (1970) Accumulation of tectonic strain in California. Bull Seismol Soc Am 60(6):1877–1896. https://doi.org/10.1785/BSSA0600061877
Shanno DF (1970) Conditioning of quasi-Newton methods for function minimization. Math Comp 24:647–656. https://doi.org/10.2307/2004840
Shen Z-K, Jackson DD, Ge BX (1996) Crustal deformation across and beyond the Los Angeles basin from geodetic measurements. J Geophys Res 101(B12):27957–27980. https://doi.org/10.1029/96JB02544
Stone M (1974) Cross-validatory choice and assessment of statistical predictions. J Royal Stat Soc Series B (Methodological) 36(2):111–133. https://doi.org/10.1111/j.2517-6161.1974.tb00994.x
Takamatsu N, Muramatsu H, Abe S, Hatanaka Y, Furuya T, Kakiage Y, Ohashi K, Kato C, Ohno K, Kawamoto S (2023) New GEONET analysis strategy at GSI: daily coordinates of over 1300 GNSS CORS in Japan throughout the last quarter century. Earth Planets Space 75:49. https://doi.org/10.1186/s40623-023-01787-7
Terakawa T, Matsu'ura M (2010) The 3-D tectonic stress fields in and around Japan inverted from centroid moment tensor data of seismic events. Tectonics 29:6. https://doi.org/10.1029/2009TC002626
The Geological Survey of Japan, National Institute of Advanced Industrial Science and Technology (2023) Active fault database of Japan. https://gbank.gsj.jp/activefault/index. Accessed 1 Nov 2023
The Headquarters for Earthquake Research Promotion (2001) Evaluation of Arima-Takatsuki fault zone. https://www.jishin.go.jp/main/chousa/katsudansou_pdf/76_arima-takatsuki.pdf. Accessed 20 June 2024 (in Japanese)
Tibshirani R (1996) Regression shrinkage and selection via the Lasso. J Royal Stat Soc Series B (Methodological) 58(1):267–288. https://doi.org/10.1111/j.2517-6161.1996.tb02080.x
Tsuji H, Hatanaka Y, Hiyama Y, Yamaguchi K, Furuya T, Kawamoto S (2017) Twenty-year successful operation of GEONET: What's next? J Geospatial Inf Authority Jpn 129:85–111. https://doi.org/10.57499/JOURNAL_129_10
Yabuki T, Matsu'ura M (1992) Geodetic data inversion using a Bayesian information criterion for spatial distribution of fault slip. Geophys J Int 109(2):363–375. https://doi.org/10.1111/j.1365-246X.1992.tb00102.x
Yano K, Kano M (2022) l_1 trend filtering-based detection of short-term slow slip events: application to a GNSS array in southwest Japan. J Geophys Res Solid Earth 127(5):e2021JB023258. https://doi.org/10.1029/2021JB023258
Zou H, Hastie T (2005) Regularization and variable selection via the elastic net. J R Stat Soc Ser B (Stat Methodol) 67(2):301–320. https://doi.org/10.1111/j.1467-9868.2005.00503.x

Publisher's Note